UC San Diego
UC San Diego Previously Published Works

Title

Fast Diagnosis of Failure Mechanisms and Lifetime Prediction of Li Metal Batteries

Permalink

https://escholarship.org/uc/item/6x69j3px

Journal

Small Methods, 5(2)

ISSN

2366-9608

Authors

Gao, Ningshengjie

Abboud, Alexander W

Mattei, Gerard S

et al.

Publication Date

2021-02-01

DOI

10.1002/smtd.202000807

Peer reviewed

FULL PAPER

small
method
www.small-methods.com

Check for
updates

Fast Diagnosis of Failure Mechanisms and Lifetime Prediction of Li Metal Batteries

Ningshengjie Gao, Alexander W. Abboud, Gerard S. Mattei, Zhuo Li, Adam A. Corrao, Chengcheng Fang, Boryann Liaw, Ying Shirley Meng, Peter G. Khalifah, Eric J. Dufek, and Bin Li*

Lithium (Li) metal serving as an anode has the potential to double or triple stored energies in rechargeable Li batteries. However, they typically have short cycling lifetimes due to parasitic reactions between the Li metal and electrolyte. It is critically required to develop early fault-detection methods for different failure mechanisms and quick lifetime-prediction methods to ensure rapid development. Prior efforts to determine the dominant failure mechanisms have typically required destructive cell disassembly. In this study, non-destructive diagnostic method based on rest voltages and coulombic efficiency are used to easily distinguish the different failure mechanisms— from loss of Li inventory, electrolyte depletion, and increased cell impedance— which are deeply understood and well validated by experiments and modeling. Using this new diagnostic method, the maximum lifetime of a Li metal cell can be quickly predicted from tests of corresponding anode-free cells, which is important for the screenings of electrolytes, anode stabilization, optimization of operating conditions, and rational battery design.

1. Introduction

Rechargeable lithium (Li)-ion batteries have become ubiquitous in our daily lives powering most portable electronic and optoelectronic devices throughout the world.[1] However, widespread adoption of electric vehicles will require higher energy batteries that can further reduce cost beyond current levels for Li-ion batteries.[2] To better enable the next generation of electric vehicles,

Dr. N. Gao, Dr. A. W. Abboud, Dr. B. Y. Liaw, Dr. E. J. Dufek, Dr. B. Li
Energy Storage & Advanced Transportation Department
Idaho National Laboratory
Idaho Falls, ID 83415, USA
E-mail: Bin.li@inl.gov
G. S. Mattei, Z. Li, A. A. Corrao, Prof. P. G. Khalifah
Chemistry Department
Stony Brook University
Stony Brook, NY 11794-3400, USA
G. S. Mattei, Z. Li, Prof. P. G. Khalifah
Chemistry Division
Brookhaven National Laboratory
Upton, NY 11973, USA
Dr. C. Fang, Prof. Y. S. Meng
Department of NanoEngineering
University of California San Diego
La Jolla, CA 92093, USA

The ORCID identification number(s) for the author(s) of this article can be found under https://doi.org/10.1002/smtd.202000807.

the U.S. Department of Energy aims to advance battery technology to achieve a specific energy of 500 Wh kg^{-1}, and a life of 1000 cycles.[3] To meet these targets, large improvements in specific energy are critically needed.

One promising route to increase the specific energy of batteries is to switch to Li metal anodes. Batteries with Li metal serving as the anode can deliver exceptionally high energy densities,[4] because of their advantages in having the lowest redox potential (-3.04 V vs standard hydrogen electrode) and a high theoretical specific capacity (3860 mAh g^{-1}). Studies suggest that the energy density of batteries can be doubled or tripled relative to present technologies using Li metal anodes.[2]

However, the practical applications of Li metal anodes are severely hindered by their rapid failure. This failure is primarily driven by parasitic reactions between Li metal and electrolyte. The common signatures of failure are the formation of dead/isolated Li, which is electrically disconnected from the bulk Li metal during uneven stripping on the anode surface,[5,6] the dendritic or mossy Li, which is induced by inhomogeneous distributions of space charge[7] on the anode surface which arise from uneven anode surfaces or cracks in the solid electrolyte interphase (SEI).[8] Rechargeable Li metal batteries (LMBs) cannot be deployed in automotive applications unless lifetime limitations are overcome.

Numerous strategies have been explored to successfully extend the lifetime of LMBs. These include developing novel electrolytes that produce more stable SEI layers, creating artificial SEI layers on the Li metal surface, and applying external pressures.[9] While these and other methods provide pathways for improving the lifetime of batteries, none of them have succeeded in meeting industrial performance targets. In order to accelerate the development of viable LMB technologies, it is critically important to develop diagnostic techniques that can rapidly and easily identify the primary cause of battery failure and that can make useful predictions about the lifetime of a cell based on data collected early in its lifetime (instead of waiting long times for cells to reach their actual failure point before getting feedback).

There are three commonly seen battery failure mechanisms for LMBs that reduce the capacity of a cell over its lifetime.[10]

**ADVANCED
SCIENCE NEWS**

www.advancedsciencenews.com

**small
methods**

www.small-methods.com

These are electrolyte depletion (ED), a loss of Li inventory (LLI), and increased cell impedance (ICI).[2] It is understood that ED mainly arises from continuous parasitic reactions between the Li metal anode and the electrolyte. Gas generation at the positive electrode due to electrolyte decomposition at higher voltages is another cause of ED.[2,11] LLI occurs due to the formation of inaccessible Li metal, such as SEI and dead Li.[2,5] ICI is attributed to the development of porous and resistive electrode surface due to SEI growth and/or an electrolyte conductivity decrease in the situation of ample electrolyte and Li inventory. ICI will lead to reduced active material utilization, especially at high current densities, which can be recovered during subsequent tests at low current densities.

The most straightforward ways to distinguish between these three cell-failure mechanisms are all either time-consuming or material intensive, making the development of novel fast and non-destructive electrochemical diagnostics of failure mechanism an important goal. Both ED and LLI failure mechanism diagnoses are currently done using traditional recovery experiments, in which a cell that has failed will be tested to see if its lost capacity can be recovered by adding more electrolytes (for ED) or by replacing cycled anodes with new Li metal (for LLI).[2] ICI failure is typically very slowly interrogated by performing repetitive reference performance tests (RPTs) at low current densities.[12] It should also be noted that these standard approaches are more difficult to adopt to the testing of consumer-owned products, due to either the need to disassemble the cell into its components or to the need to carry out slow electrochemical testing procedures that will take days to complete.

In addition to diagnosing failure mechanisms, a good diagnostic test will also be able to provide robust predictive insights into the lifetime of the cell from data collected over a limited set of initial electrochemical cycles. Some types of early-fault detection studies that aim to predict failure mode include techniques such as gas sensing, self-discharge current measurements, and online impedance spectroscopy measurements.[11,13] These measurements require advanced instrumentation that are difficult to readily integrate into commercial products. Simpler measurement methods, such as the electrochemical characterizations of rest voltage and voltage shape, have previously been used as indicators of changes in cell chemistry mainly in Li‖Li symmetric cell.[14,15] The rest voltage as a signal for ICI (dead Li formation) was applied in full cell study,[6] but using rest voltage to identify the three failure mechanisms in full cells has not been fully investigated.

Conventional lifetime evaluation for LMBs through long-term cycling is a time-consuming and expensive task and it is not practical in every case. In the absence of long-term cycling data, it is generally challenging to make accurate predictions of battery lifetimes because the cells may die due to many different failure modes. If a dominant failure mode can be identified through diagnostic testing, it becomes easier to make lifetime predications and thus allow earlier development of technological advances. This can be facilitated by accelerated lifetime testing (ALT), which is conducted by promoting degradation under aggressive operating conditions without changing the dominant failure mechanism. ALT has been widely used in many fields such as traditional Li-ion batteries, solid-oxide fuel cells, proton-exchange membrane fuel cells, and solar

cells.[16–18] By limiting the cell failure mechanism to one cause, it is possible to quickly predict the lifetime of LMBs using ALT. Furthermore, this knowledge can be used to rationally design cells which could balance the specific energy and lifetimes by changing the relative amounts of key cell components (e.g., electrolyte, anode, cathode).

In this study, based on the rational cell design, we developed and validated a purely electrochemical early-detection method for distinguishing between different cell failure mechanisms. This method involves monitoring changes in the cell rest voltage and coulombic efficiency (CE), which can readily be tracked during the cycling of cells in both a laboratory and a commercial setting, and is well validated through synchrotron x-ray diffraction (XRD) and microscale modeling. Furthermore, an ALT approach to quickly predict the maximum lifetime of LMBs with anode-free Li-metal cells under the Li-limiting circumstance is proposed and validated against experimental data. The approaches described here are safe, cost-effective, non-destructive, and reliable, and provide substantial advantages in these properties over existing cell failure diagnostic methods.

2. Results and Discussion

Three different types of LMB cells were designed rationally to fail with each of the common LMB cell failure mechanisms (ED, LLI, and ICI). These cells were constructed with cathodes of $LiNi_{0.8}Mn_{0.1}Co_{0.1}O_2$ (NMC811) due to its high specific capacity and voltage. These expected cell-failure mechanisms were validated through traditional recovery experiments and RPT cycles. A simple, non-destructive, and real-time electrochemical diagnostic method that can distinguish between these failure modes was proposed based on the electrochemical test data collected for these three types of cells. Additionally, this approach was further validated with both modeling and additional experimental characterizations.

2.1. LLI-Dominated Cell Decay in Cu‖NMC811

An anode-free Li-metal cell (Cu‖NMC811) with flooded electrolyte was used to promote failure by LLI by 1) not providing excess Li and 2) providing sufficient electrolyte to avoid capacity loss due to ED. As shown in **Figure 1**A, capacity fading for Cu‖NMC811 cell occurs from the first cycle. Adding more electrolyte to a dead Cu‖NMC811 cell (at Cycle 32) and running RPT 1 cycles cannot recover the capacity, ruling out ED and ICI as the main reasons for the capacity loss. In contrast, replacing the bare Cu anode with a Li metal anode (at Cycle 36) allows 93% of the original capacity (measured at the end of the third formation cycle) to be recovered. This behavior indicates that the Cu‖NMC811 cell died primarily due to LLI.

To further confirm this, differential capacity (dQ/dV) curves were generated (Figure 1B) using both formation cycle and RPT cycle data collected at low charge/discharge rates in order to show the progressive kinetic changes from the beginning of life. An RPT cycle was performed following the formation cycles and after every 20 aging cycles for the duration of the cycle life test. The formation dQ/dV curve exhibits four redox

**ADVANCED
SCIENCE NEWS**

www.advancedsciencenews.com

**small
methods**

www.small-methods.com
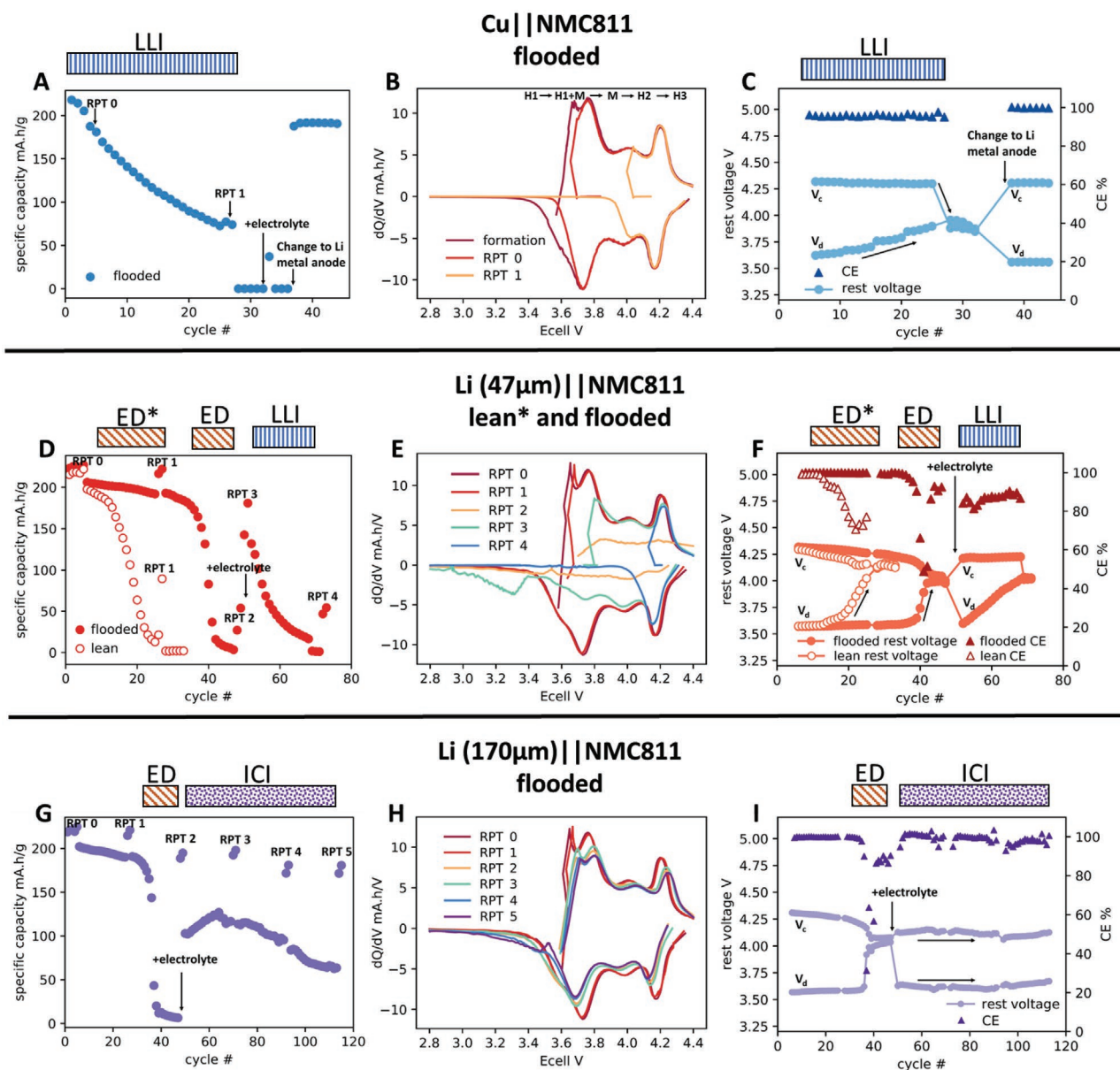
Figure 1. Capacity fading (A) for Cu‖NMC811 cell (flooded), and its corresponding dQ/dV curves (B), and rest voltages and CE values over cycling (C). D) Capacity fading for Li (47 µm-thick)‖NMC811 cell under flooded and lean electrolyte conditions, E) dQ/dV curves for the flooded Li‖NMC811 cells, and F) rest voltages and CE values of flooded and lean Li‖NMC811 cells over cycling. Capacity fading for Li (170 µm-thick)‖NMC cell under flooded electrolyte condition (G), dQ/dV curves (H), and corresponding rest voltages and CE values over cycling (I). LLI, loss of Li inventory; ED, electrolyte depletion for flooded-electrolyte cell; ED*, electrolyte depletion for lean-electrolyte cell; ICI, increased cell impedance.

peaks during charging associated with phase transitions which from low voltage to high are: hexagonal (H1) stage to a mixed stage of monoclinic (M) and H1, the mixed stage to M, M to the second hexagonal phase (H2), and to the third hexagonal phase (H3).[19,20] The lower-voltage peaks for RPT 0 and RPT 1 curves progressively disappear in both charge and discharge stages (Figure 1B). This is because LLI causes the NMC cathode to be unable to be fully relithiated during cell discharge, preventing it from returning to the low state of charge (SOC) originally exhibited by the pristine cell, both at normal current density and at the low current density of the RPT cycles. All remaining dQ/dV peaks overlap well with those of the formation cycle,

suggesting there were no significant increases in cell impedance that occurred during testing.

A schematic in **Figure 2**A shows the expected changes of Cu‖NMC811 cell during cycling when capacity loss is dominated by the LLI mechanism. In those cells, the Li in the cell comes only from the NMC cathode. During the charging process, Li from the cathode is plated onto the Cu current collector. However, due to the formation of SEI and dead Li, only part of the plated Li metal on the Cu surface can be stripped back to the cathode during discharging, and the Li inventory becomes the limiting factor starting from the first cycle in Cu‖NMC811 cells. The SOC at the end of charge remains constant or perhaps
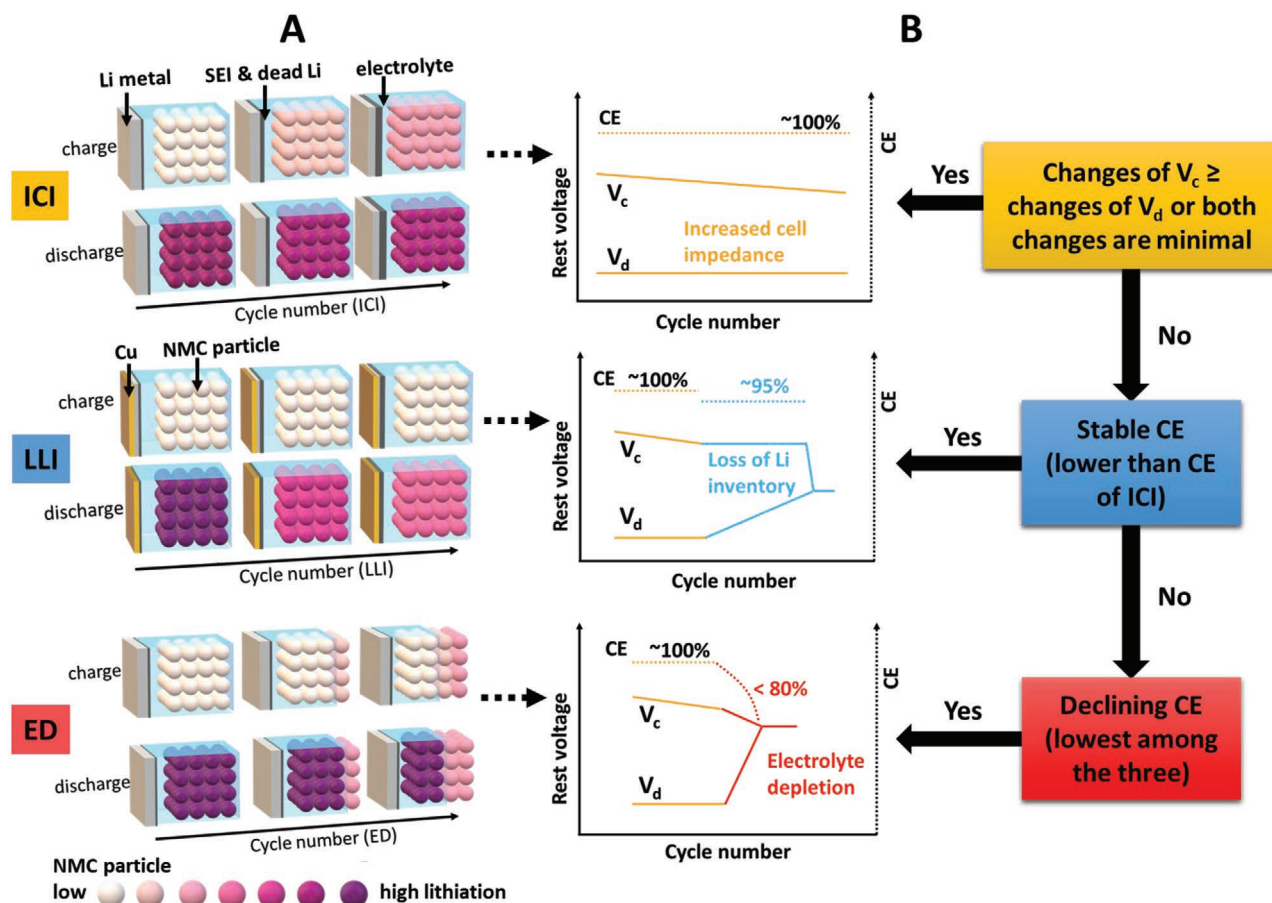
Figure 2. A) Schematic illustration of the hypothetical changes of cathode SOC, anode (Li metal and anode free), and electrolyte amount during the LLI, ED, and ICI. B) The diagram demonstrating fast diagnosis of failure mechanisms using rest voltages and CE.

slightly reduced due to the increased cell impedance because there is nothing to inhibit the delithiation of the cathode. However, the Li inventory is reduced during each cycle, as is the amount of Li available for cathode lithiation, which leads to a continuously increasing SOC at the end of discharge.

These changes in the SOC limits during each aging cycle should be reflected in the rest voltages measured for the cell at the end of each charge (V_c) and discharge (V_d) period, which is shown in Figure 1C. In LMBs, the cell rest voltage is wholly dependent on the Li content of the cathode because the redox potential of the Li metal anode remains constant. As is expected, it is found that the charge rest voltage (V_c) remains relatively stable (since the cathode can always be nearly fully delithiated) while the discharge rest voltage (V_d) continually increases with cycle number (since maximum degree of cathode lithiation decreases as the Li inventory decreases). The absence of an obvious capacity change after adding more electrolytes and running RPT cycles suggests that during the cycling of these Cu‖NMC811 cells, the contributions of ED and ICI to the capacity loss are small enough to be negligible. In addition, the CE value during the LLI period stays constant around 95.7%. Upon replacing Cu with fresh Li metal anode, the CE value increases to above 99.7%. Because the Li inventory is rejuvenated, the CE is increased, and V_d and V_c both recover to values comparable with the first aging cycle.

2.2. ED-Dominated Cell Decay in Thin Li‖NMC811

Almost complete capacity loss due to ED could be observed in Li(47 µm)‖NMC811 cells under both lean- and flooded-electrolyte conditions. The cells showed minor capacity fading in the early cycles (Figure 1D) followed by a rapid decrease in capacity after about 10 cycles (lean electrolyte) or 35 cycles (flooded electrolyte). It is expected that larger electrolyte amount will delay failure when ED mechanism is dominant,[21] and the observed electrolyte dependence on the lifetime of these two cells indirectly confirms that the cell failure mode is primarily ED. Direct proof that the failure mechanism was ED was obtained by recovery experiments. When 48 µL of additional electrolyte was injected to the flooded cell after failure (Cycle 49), the cell capacity recovered to 80% before decaying further with additional cycling. For the flooded cell, the dQ/dV curves generated by RPT 0 and RPT 1 (Figure 1E) overlap well and exhibit the same four redox peaks on both charge and discharge, indicating no significant impedance increases for the cell over this period. The dQ/dV curve for RPT 2 shows reduced peak intensities which is a signature of a reduced utilization of cathode active material. Nevertheless, after adding more electrolytes, the dQ/dV curve corresponding to RPT 3 exhibits recovered peak intensities at higher-voltage range (above 3.9 V), indicating that cathode utilization has recovered, and that the reduced peak

intensities for RPT 2 were caused by ED. Additionally, another parallel cell with lean electrolytes was stopped after substantial capacity drop, and its anode shows partial pulverization (Figure S1A, Supporting Information). A large amount of native Li metal is still observable (36.4 out of 47 µm), suggesting the cell was mainly suffering from ED.

Based on previous studies, electrolyte solvents more rapidly decompose at the cathode at high voltages than at low voltages.[22] Thus, the expected failure behavior will (Figure 2A), to a first approximation, involve the more consumption of electrolyte during the charge rather than the discharge period. With continuous cycling, more active material at the cathode becomes isolated from the electrolyte during the charging process due to gradual ED, and these portions of the cathode cannot be effectively utilized during subsequent discharging period except through very slow solid–solid Li ion exchange and diffusion processes. Ultimately, the maximum and minimum SOC limits should gradually decrease and increase after charge and discharge, respectively. Moreover, the change in the SOC at the end of discharge is expected to be more pronounced because much more electrolytes are lost during charging, leading to more interparticle diffusion happening during subsequent discharging. This behavior is also predicted by microscale modeling simulations, discussed in more detail later.

The ED-driven changes in cathode SOC limits can be reflected in changes in the cell rest voltage, as was the case for LLI-driven changes. As shown in Figure 1F, a key characteristic of capacity loss (lean: cycles 14–26; flooded: cycles 38–43) due to ED is that V_d increases very rapidly in the region where the last 25% of the reversible cell capacity is lost. V_c also substantially decreases in this region, though not nearly as much as V_d. Within this period, the CE drops substantially, to less than 80% with the lowest value below 50%. After the addition of fresh electrolyte, as the cycling continues, the dQ/dV peaks (Figure 1E) for RPT 3 and RPT 4 gradually vanish starting from low-voltage peaks. These changes are similar to those in Figure 1B, suggesting that the second capacity fade after electrolyte addition was mainly because of LLI. During LLI, the rest voltages (Figure 1F) display the same trend as those in Cu‖NMC811 cell (Figure 1C), and the CE returns to a relatively stable stage with an average value of 86.7%. The CE during LLI period is much smaller than that before cycle 40 in Figure 1F, due to a lack of excess Li source to compensate the loss.[23] After the cell died, as shown in Figure S1B, Supporting Information, the anode was completely pulverized, with considerable thickness increase and no obvious native Li observed, further proving that the cell failure was mainly driven by LLI.

In summary, the Li‖NMC811 cells built with thin Li metal foil (47 µm) initially fail through ED, both under lean-electrolyte and flooded-electrolyte conditions. If the electrolyte is replenished, failure then occurs through LLI. If other failure modes are to be examined, test cells will need to be built with thicker Li metal anodes as is discussed next.

2.3. ICI-Dominated Cell Decay in Thick Li‖NMC811

To allow a Li‖NMC cell to operate for more than ≈30–70 cycles accomplished in tests of ED and LLI failure, another Li‖NMC811 cell was built with a thicker Li metal anode (170 µm) and with flooded electrolyte to test failure mechanisms after more extensive cycling (Figure 1G). As was seen for cells with thin Li anodes, the first significant capacity fade happened due to ED after cycle 36. After adding an extra 48 µL of electrolyte at cycle 47, the capacity recovered to 88% during the low-current density RPT 2 cycle. The capacities for the subsequent RPT cycles remained similar to that for RPT 2. In contrast, the capacity for the high-current aging cycles dropped to about half of the capacity observed in RPT 2. This large current-dependent capacity difference is primarily caused by ICI. When the cells are being cycled, it is expected that parasitic reactions will destroy active material at both electrodes, thereby resulting in a buildup of cell impedance by formation of resistive SEI, dead Li, and cathode electrolyte interphase (CEI), as shown schematically in Figure 2A. These resistive layers will hinder ion transport and increase cell overpotential, thus causing significant observed capacity fading at high current densities due to the reduced utilization of active material that occurs when voltage cutoffs are constant.[24] The consumption of electrolyte, including both salt and solvent, may affect the composition of SEI[25] and the conductivity of the electrolyte (Figure S2, Supporting Information), which may also change the impedance of the cell.

During RPT cycles at low current densities, the ICI-induced overpotentials are minimized, enabling nearly complete utilization of the cathode materials. As shown in Figure 1H, the dQ/dV plots for all RPT cycles exhibit complete redox peaks with similar intensities. However, the gradually shifting peak voltages and slightly reduced peak intensities still reflect the ICI effect. As shown in Figure 2A, with increasing cell impedances, the cathode SOC at 4.4 V (and thus V_c) continually decreases. This standard 4.4 V upper limit during charging is chosen to minimize the side reactions such as electrolyte decomposition and surface reaction of NMC that occur much more rapidly at voltages higher than this.[26] However, at the end of discharge, the cutoff voltage of 2.8 V is well below the thermodynamic equilibrium voltage for NMC811 at low SOC (≈3.4 V shown in dQ/dV curves for RPT cycles of Figure 1H). Since the 2.8 V lower limit was selected to accommodate with kinetically driven cutoffs rather than a limit in the NMC811 thermodynamic potential, the NMC811 SOC at the end of discharge (and thus V_d) remains relatively constant throughout the cycling despite the increases in cell impedance. For Li‖NMC cells (Figure 1I), the values of V_d and V_c both change continually during earlier cycles where the specific capacity is slowly decreasing due to the effect of ICI, with V_c decreasing a little more quickly than V_d increases. After reinjecting extra electrolyte, the V_c and V_d split apart widely in Figure 1I and do not display significant change afterward. Overall, in the whole ICI process (excluding ED cycles), the CE stays relatively constant with values that remain near 100%. Even though the overall cell capacity decreases from around 50% to 25% of the initial capacity due to ICI effects when cycled after electrolyte addition, the values of V_c and V_d stay nearly constant.

At least five coin cells were repeated for each failure mechanism, and they show similar performances. The charge and discharge curves for each failure mechanism are shown in Figure S3A–C, Supporting Information. Coin cells cycled at different rates (1 C and C/2) were also tested as shown in Figure S4, Supporting Information.

**ADVANCED
SCIENCE NEWS**

www.advancedsciencenews.com

**small
methods**

www.small-methods.com

2.4. Fast Diagnosis of Different Failure Mechanisms

Based on the results from the previous sections, the signatures of three different dominant failure mechanisms (ED, LLI, and ICI) were identified in cells designed to exhibit different failure modes (Cu∥NMC811, thin Li∥NMC811, thick Li∥NMC811). Although all of these mechanisms contributing to the loss of cell capacity may be simultaneously operative in actual cells, the present data suggest that there is typically only one dominant failure mode (even if this mode may be different at different periods during testing). Each of these three dominant failure mechanisms can be distinguished and validated based on a comprehensive comparison on the dQ/dV curves and experimental-cell recovery processes. However, in practical application, it may not be realistic to open and recover the cells, or to perform the long RPT cycles. Therefore, a more accessible method is needed to quickly separate the different failure mechanisms without additional tests. Herein, inspired by the actual cell-testing results, we used the changes in V_c and V_d together with CE as a way of differentiating the three dominant failure mechanisms.

As illustrated in Figure 2B, by comparing the changes of V_c and V_d, if the decrease of V_c is not smaller than the increase of V_d (or the changes of V_c and V_d are both minimal), the corresponding failure mechanism is ascribed to ICI. In this situation, the CE is constant and close to 100%, which is the highest among the three failure mechanisms. In most cases, the LMBs start with an impedance buildup, partially due to SEI/dead Li layer formation, and evolution from dense to porous structures,[27] rather than ED or LLI during these early cycles. However, if the decrease of V_c is minimal and the increase of V_d is pronounced, CE should be taken into consideration as a second parameter. If CE exhibits a relatively constant trend, but the value is smaller than CE during ICI, then the cell is experiencing a dominant failure mechanism of LLI. Otherwise, if CE shows a fast-declining trend (to less than 80% in the current experiment), then the dominant mechanism should be ED. In our work, the absolute CE value depends on many factors, such as electrolyte selection and charge/discharge current density. Thus, as the diagnostic criteria, the absolute CE values were not directly compared for the three failure mechanisms. By recording the rest voltage value and CE during cycling, the dominant failure mechanism of the cells can be determined in real time, allowing a facile diagnosis and hence a means to readily assess new technological solutions for improving LMB performance.

## 2.5. Validation of Diagnostic Methods

2.5.1. Synchrotron XRD

The use of synchrotron XRD to probe the cycling of batteries differs from electrochemical testing in some keyways. First, the cathode SOC in XRD studies was determined based on direct measurements of the unit cell volume and thus will not suffer from any uncertainty associated with overpotentials. This contrasts with measurements of V_c and V_d, where the time period of relaxation is expected to affect the measured voltage. In this

study, rest voltages were recorded at the end of 15 min rest, when the cell voltage did not significantly change over time and the corresponding dV/dt value was near 0 (Figure S3D,E, Supporting Information). Second, using high-energy lateral mapping (HELM) methods that will be described in more detail elsewhere, it is possible to explore the spatial inhomogeneity of the cathode films, in contrast to electrochemical measurements which only return the average response for the cell as a whole. As such, synchrotron XRD studies provide an important complement to electrochemical measurements that allow the expected cell behavior under different cell failure mechanisms (Figures 1 and 2) to be assessed.

In order to probe cell failure with diffraction methods, two series of samples were prepared for ex situ synchrotron HELM studies. The first series was designed to fail through ED (samples 1–7) and the second through LLI (samples 8–12). In each series (**Figure 3**), samples were stopped at different stages in the lifetime of the cell, both at the end of the charge (upper maps) and the end of the discharge (lower maps) segments, with the last data collected on a sample without significant capacity and thus not distinguishable as a charge or discharge endpoint (center maps). The capacities and the corresponding cycle numbers for these 12 samples at the point that electrochemical testing was stopped are listed in Table S1, Supporting Information. The circular maps plot the position-dependence of the SOC of cathode films extracted from these test cells. The circular maps are labeled with the average SOC for the film as a whole with the exception of sample 8, whose results were not representative due to problems with the cathode film preparation, as detailed in Figure S5, Supporting Information. These issues also resulted in sample 8 being the only sample not to have a homogeneous SOC distribution across the area of the cathode disc.

The SOC evolution observed through XRD studies of Li∥NMC samples (samples 1–7) is fully consistent with both the measured (Figure 1F) and expected (Figure 2A) rest voltage behavior for samples whose failure is dominated by ED. Samples 5 and 6 were experiencing ED. During the ED processes, at the end of discharge, the SOC of sample 6 increased significantly by more than 40% compared with sample 2 and 4. At the end of charge, the SOC of sample 5 expressed a smaller decrease by about 14% compared to samples 1 and 3. The cell after failure (sample 7) has an SOC of 71% that indicates that the failed cell ends up at a high SOC, and the SOC change at the end of discharge is more significant than those at the end of charge during ED process, which agrees well with the changes in rest voltages observed in previous experiments (Figure 1F).

It is also found that the SOC evolution observed through XRD studies of Cu∥NMC samples (samples 8–12) is fully consistent with both the measured (Figure 1C) and expected (Figure 2A) rest voltage behavior for samples whose failure is dominated by LLI. The SOC measured for samples at the end of discharge (samples 9 and 11) increases rapidly and consistently at the beginning of the cell lifetime, as was observed for V_d (Figure 1C). Similarly, the SOC measured at the end of the charge after 18 cycles (sample 10) remains very high. The SOC after complete failure due to LLI (sample 12) is 62.5%, a value which represents a high SOC though not quite as high as the value of 71% seen for failure due to ED.
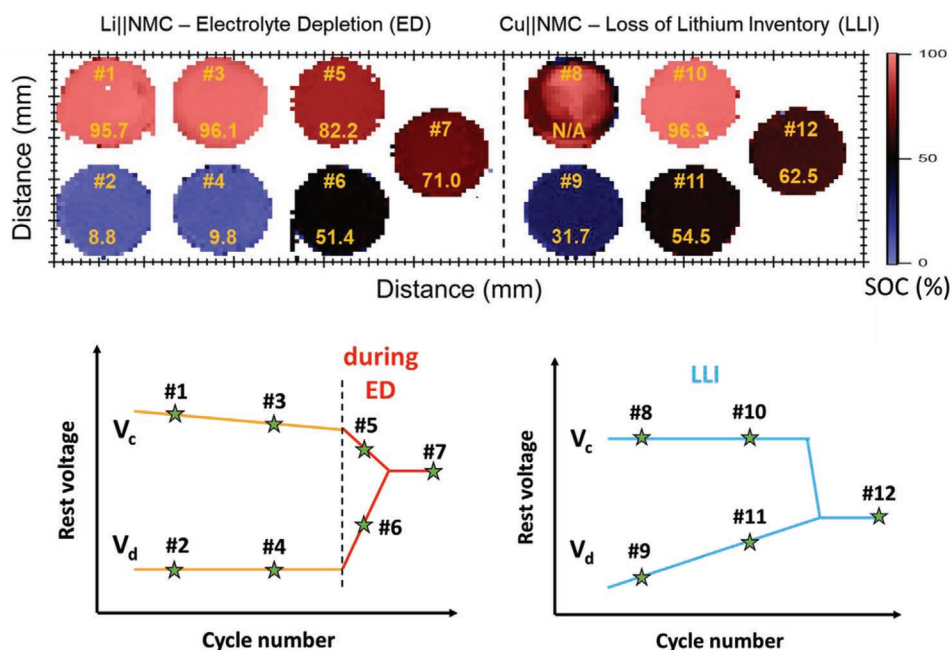
Figure 3. Ex situ Synchrotron XRD analysis results show the SOC distribution for each cathode sample. Average SOCs are shown on each sample plot. Samples 1–7 were collected from Li‖NMC811 cells suffering ED. Samples 8–12 were collected from Cu‖NMC811 cells experiencing LLI.

These direct XRD measurements of the cathode structure confirm that the electrochemically measured changes in V_c and V_d are representative of the actual changes in cathode SOC that occur during cycling. In addition, these XRD measurements indicate that the cathodes remain homogeneous throughout the lifetime of these cells across the area of the films, which provides a basis for the modeling below.

2.5.2. Microscale Modeling

Besides changes in SOC or rest voltage, as displayed in Figure 2, changes in CE over cycling is another key parameter used to distinguish ED from LLI and ICI. Substantially decreasing CE only occurs during the ED, as was validated through modified microscale modeling[28] (**Figure** 4A; see details in Supporting Information). Under the flooded or moderate electrolyte condition, reducing the amount of electrolyte does not change CE or cell chemistry. Thus, the model started with lean electrolyte condition (≈ 2.06 g Ah^{-1}), where the amount of electrolyte barely fills the cathode pores. As shown in Figure 3 (samples 5 and 6), during the ED, the SOC distribution across the areas of cathode films is uniform, suggesting the model could be run by removing electrolyte along the cathode lateral direction in Figure S6, Supporting Information.

During charging, as electrolyte is removed (consumed) from the cathode collector side due to higher voltage, Li ions are isolated in the end of the cell nearest the current collector due to slow interparticle Li ion transport with selected simulation results shown in the left column of Figure 4B (complete results see Figure S7, Supporting Information). Similarly, for the discharging cycle the lithium ions cannot be fully transported to

the current collector side of the cathode as shown in the right column of Figure 4B. The Li concentration in NMC particles nearest the current collector is larger than that nearest the anode at the end of charge, and the opposite is true at the end of discharge. The modeling results are consistent with the schematics corresponding to ED process in Figure 2A. After a charge/discharge cycle, the average Li concentration in the cathode was used to calculate an average rest voltage based on the open circuit potential function. As shown in Figure 4C, the results show a drop and an increase after charge and discharge, respectively, in the rest voltage as electrolyte is removed, nearly consistent with the experimental results in Figure 1F. The CE was calculated as the ratio of total flux of Li ions across the cell during the cycle. The lithium ion concentration of the cell after discharge was used for the initial condition of the cell for the following charging process. Then the difference in the total lithium flux was calculated to represent the capacities for charging and discharging processes, and corresponding CE values are calculated and shown in Figure 4C. The simulated CE shows a non-linear decrease as electrolyte is removed from the system, which matches well with the experimental results in Figure 1F.

Notably, the electrolyte depletion mentioned in this study is not limited to a complete dry-out, but can be expanded to a situation of isolated or dead electrolyte contained in the porous cycled anode and the cathode, yet disconnected from the bulk electrolyte (Figure S8, Supporting Information). The isolated electrolyte accelerates the ED in addition to reaction consumption, and the amount can be amplified with continuously formed pores on the Li metal.[27]

By and large, the fast-diagnostic method shows good agreement with all the previous validations, highlighting the feasibility of using the changing trend of rest voltage and CE to
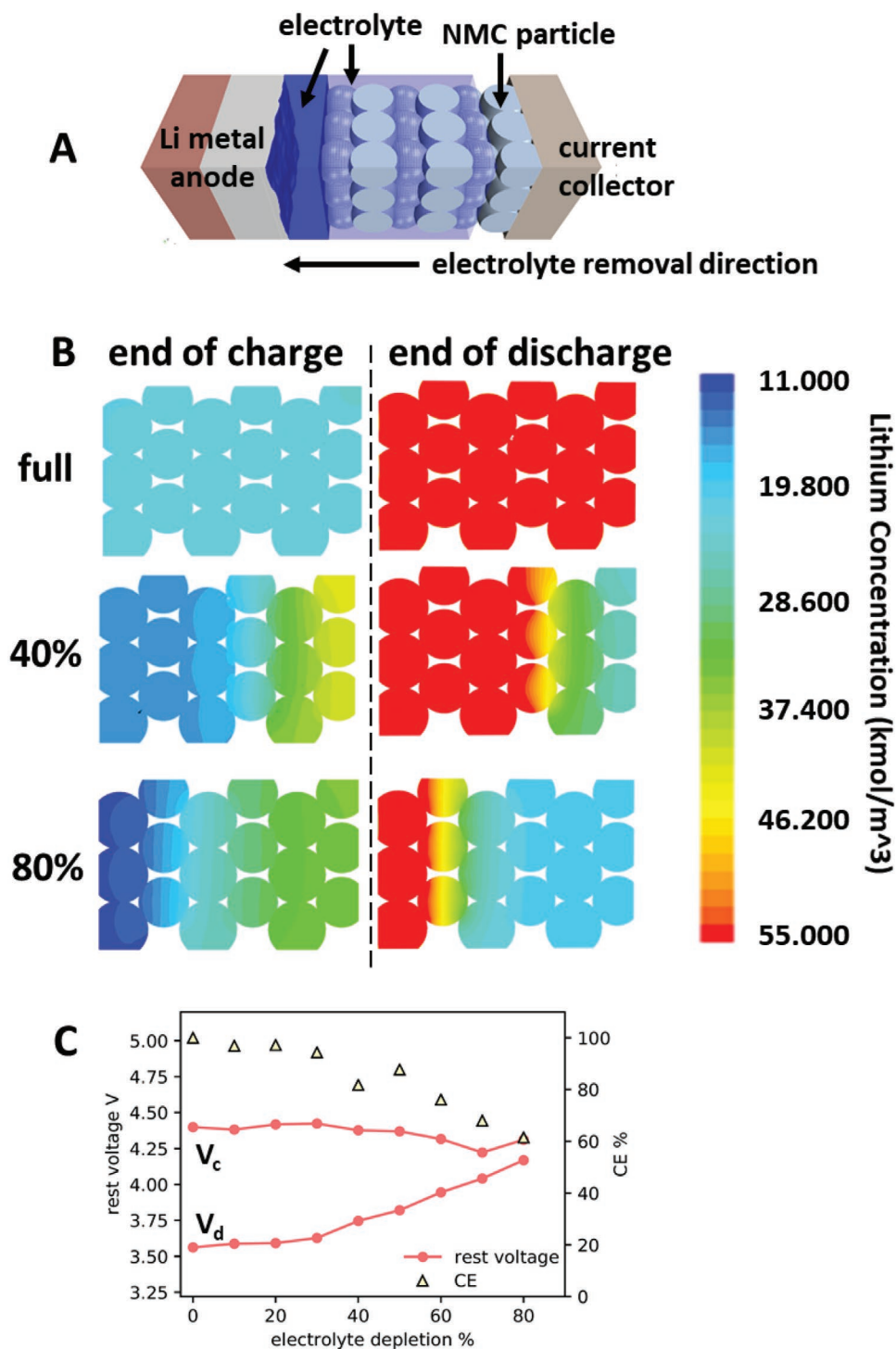
Figure 4. A) Schematics showing microscale Li‖NMC811 cell and electrolyte depletion from the cathode current collector side. B) Selected modeling results for Li concentration in the cathode active material after charging and discharging with electrolyte removed by 0, 40%, and 80%; the current collector locates at the right side of each plot. C) The simulated rest voltages and CEs as a function of electrolyte depletion percentage.

distinguish different cell-failure mechanisms. This method can be used in battery-management systems to quickly detect early failure without a need for additional tests. This could also facilitate the development of battery chemistries by highlighting the dominant failure mechanism.

2.6. Li‖NMC811 Maximum Lifetime Prediction Using ALT

Lifetime prediction has been as important as the development of battery chemistry to estimate potential battery performance without conducting prolonged cycling. However, due to the

various failure mechanisms for each actual cell, attention must be paid when comparing experimental and predictive results. With the well-established fast-diagnostic method, the validation of a lifetime prediction becomes easier under one predefined dominant failure mechanism. Using Cu‖Li cells to screen potential electrolyte candidates has been commonly used in previous studies.[29] In this section, the maximum lifetime of Li‖NMC811 cells was predicted by Cu‖NMC811 cells, given fixed cathode and electrolyte under the Li-limiting condition, i.e., LLI is the ultimate failure mechanism. This means such prediction is based on several assumptions: The electrolyte is always enough, ICI is ignored, and the Li-consumption rate on the Cu and Li metal anodes is the same.

For a typical LMB, the Li metal anode provides sufficient Li during the early life. Excess Li (and assuming plenty electrolyte with negligible ICI) results in a high CE close to 100% and relatively stable cell capacity. However, once the Li metal is used up at the anode side, the accessible Li only comes from the cathode, leading to a lower CE and obvious capacity decay. Therefore, a two-stage LLI model for LMBs was proposed: Stage 1, during which Li is in excess and the Li loss/cycle is nearly constant, and stage 2, during which the Li metal anode is totally consumed, the Li loss/cycle follows an exponential way similar to the Cu‖NMC811 cells where all Li originate from the cathode. As a result, the cycle life for the first stage is controlled by both the thickness of the Li metal anode and the Li consumption rate while the cycle life for the second stage is determined by the Li content in the cathode (or Cu‖NMC811 initial capacity) and the Li consumption rate. The Li consumption rate can be obtained from the CE of the corresponding Cu‖NMC811 cell.

For stage 1, the maximum lifetime can be calculated as follows:

$$\text{Stage 1}: x_1 = H / \left(C \times (1 - CE\%) \times M \times 10 / (F \times d \times s) \right) \tag{1}$$

where H: total thickness of Li metal (μm); C: capacity of Cu‖NMC811 (mA h); M: molar mass of Li (6.941 g mol^{-1}); F: Faraday's constant (26.801 Ah mol^{-1}); d: density of Li metal (0.534 g cm^{-3}); s: projected surface area of cathode (cm^2); the 10 is for unit conversion.

For stage 2, the lifetime was estimated using Equation (2), assuming the cell is not considered dead until its capacity drops to 40% of the original value:

$$\text{Stage 2}: x_2 = \log_{CE\%} 40\% \tag{2}$$

$$\text{Total predicted lifetime}: x = x_1 + x_2 \tag{3}$$

Average CE with the value of 95.7% was obtained based on the Cu‖NMC811 cell in Figure 1C, and the estimated maximum

Table 1. Predicted coin-cell maximum lifetime with 47-μm-thick Li metal and flooded electrolyte (1.6 M LiPF$_6$).

	Predicted	Actual Li‖NMC cell
Capacity of NMC811	5.5 mAh	
Li Loss/cycle (excess)	0.90 μm	
Cycle (x_1)	52	47
Li Loss/cycle (limited)	4.3%	
Cycle (x_2)[a]	20	8
Total lifetime	72 cycles	55 cycles[b]

[a]40% final capacity percentage; [b]Excluding low capacity cycles during ED.

lifetime of Li‖NMC cells was listed in **Table 1**, as calculated with Equations (1)–(3). To prove this ALT method, an actual Li‖NMC cell under the same condition was operated, as shown in Figure S9, Supporting Information, with an ultimate failure mechanism of LLI (Figure S9B, Supporting Information). RPT testing was eliminated to avoid additional variance. The maximum cycle life of stage 1 was calculated to be 52 cycles, which is longer than the actual 47 cycles (Figure S9A, Supporting Information, 48 total cycles, excluding cycles 37–43 that showed <40% of capacity retention, plus cycles 44–49 after recovery). During stage 2, the actual cell operated for eight cycles (Figure S9A, Supporting Information, cycles 50–57) before the capacity dropped to 40% of the original, which is less than the predicted cycle life of 20.

There are two possible reasons for the shortened actual lifespan during stages 1 and 2. First, the Li consumption rate obtained in anode-free cell is smaller than that in Li metal cell. The dead Li and SEI Li on both the Cu and the Li metal anode samples were quantified by titration gas chromatography.[5] According to the results listed in **Table 2**, the dead (metallic) Li/total Li ratio on the cycled Li metal anode (average of 83.9%) is higher than on the Cu current collector (average of 50.0%), indicating a larger proportion of dead Li was formed on Li metal anode. Second, resistive SEI/dead Li or CEI were formed over cycling so that the ICI cannot be disregarded. That led to a lower capacity and shorter lifetime, especially when the cell was operated at high current densities. Notably, the more stable SEI which is formed by using advanced electrolytes or pretreating the Li metal,[9] the closer the actual lifetime will be to the predicted value.

3. Conclusion

In summary, we developed a simple and reliable approach to early detect cell failure mode in real time by monitoring the

Table 2. The amount of Li in SEI and dead Li on cycled Cu and Li metal anodes.

Sample	Total amount of Li [μg]	Metallic Li [μg]	SEI Li [μg]	Metallic Li/total Li	Average ratio
Cu-1	93.878	52.197	41.681	55.60%	50.0%
Cu-2	89.414	39.765	49.649	44.47%	
Li-1	396.251	319.040	77.211	80.51%	83.9%
Li-2	363.834	317.430	46.404	87.25%	

changes in both rest voltage and CE, which was well validated through experiment and modeling. Based on one dominant ultimate failure mechanism of LLI, a validated ALT method was demonstrated to quickly predict the maximum lifetime of LMBs using the parameters obtained from corresponding anode-free cells. With these proposed fast-diagnostic and ALT prediction methods, material development on LMBs can be facilitated. The clearly identified cell-failure mechanism can quickly underscore the cell limiting factor and better connect results in cross-studies. The ALT method can be used as a fast screening tool to prefilter electrolyte and artificial SEI candidates, as well as to optimize operational conditions (e.g., temperature, voltage range, and charge/discharge current density), and has a great potential for use in areas that need high-throughput experiments. In addition, considering the amount of electrolyte, anode, and cathode used in practical Li metal cells, these methods can also shed light on a rational cell design by improving the balance between cell lifetime and specific energy. The proposed approaches can also be applied to other metal-anode batteries, like zinc, sodium, magnesium, or potassium-based batteries, which would help accelerate the development and commercialization of Li metal and potentially other metal-based batteries.

4. Experimental Section

See Supporting Information

Supporting Information

Supporting Information is available from the Wiley Online Library or from the author.

Conflict of Interest

The authors declare no conflict of interest.

[1] L. Lu, X. Han, J. Li, J. Hua, M. Ouyang, *J. Power Sources* **2013**, *226*, 272.

[2] J. Liu, Z. Bao, Y. Cui, E. J. Dufek, J. B. Goodenough, P. Khalifah, Q. Li, B. Y. Liaw, P. Liu, A. Manthiram, Y. S. Meng, V. R. Subramanian, M. F. Toney, V. V. Viswanathan, M. S. Whittingham, J. Xiao, W. Xu, J. Yang, X. Q. Yang, J. G. Zhang, *Nat. Energy* **2019**, *4*, 180.

[3] Office of Technology Transitions, Battery500 Consortium to Spark EV Innovations: Pacific Northwest National Laboratory-led, 5-year $50M effort seeks to almost triple energy stored in electric car batteries, https://www.energy.gov/technologytransitions/articles/battery500-consortium-spark-ev-innovations-pacific-northwest-national (accessed: July 2016).

[4] S. Chen, C. Niu, H. Lee, Q. Li, L. Yu, W. Xu, J. G. Zhang, E. J. Dufek, M. S. Whittingham, S. Meng, J. Xiao, J. Liu, *Joule* **2019**, *3*, 1094.

[5] C. Fang, J. Li, M. Zhang, Y. Zhang, F. Yang, J. Z. Lee, M. H. Lee, J. Alvarado, M. A. Schroeder, Y. Yang, B. Lu, N. Williams, M. Ceja, L. Yang, M. Cai, I. Gu, K. Xu, X. Wang, Y. S. Meng, *Nature* **2019**, *572*, 511.

[6] K. H. Chen, K. N. Wood, E. Kazyak, W. S. Lepage, A. L. Davis, A. J. Sanchez, N. P. Dasgupta, *J. Mater. Chem. A* **2017**, *5*, 11671.

[7] D. Lin, Y. Liu, Y. Cui, *Nat. Nanotechnol.* **2017**, *12*, 194.

[8] M. N. Parekh, C. D. Rahn, L. A. Archer, *J. Power Sources* **2020**, *452*, 227760.

[9] X. B. Cheng, R. Zhang, C. Z. Zhao, Q. Zhang, *Chem. Rev.* **2017**, *117*, 10403.

[10] M. Broussely, P. Biensan, F. Bonhomme, P. Blanchard, S. Herreyre, K. Nechev, R. J. Staniewicz, *J. Power Sources* **2005**, *146*, 90.

[11] W. Kong, H. Li, X. Huang, L. Chen, *J. Power Sources* **2005**, *142*, 285.

[12] M. Dubarry, C. Truchot, B. Y. Liaw, K. Gering, S. Sazhin, D. Jamison, C. Michelbacher, *J. Power Sources* **2011**, *196*, 10336.

[13] U. Tröltzsch, O. Kanoun, H. R. Tränkler, *Electrochim. Acta* **2006**, *51*, 1664.

[14] H. Lee, S. Chen, X. Ren, A. Martinez, V. Shutthanandan, M. Vijayakumar, K. S. Han, Q. Li, J. Liu, W. Xu, J. G. Zhang, *ChemSusChem* **2018**, *11*, 3821.

[15] K. N. Wood, M. Noked, N. P. Dasgupta, *ACS Energy Lett.* **2017**, *2*, 664.

[16] L. Shi, T. L. Young, J. Kim, Y. Sheng, L. Wang, Y. Chen, Z. Feng, M. J. Keevers, X. Hao, P. J. Verlinden, M. A. Green, A. W. Y. Ho-Baillie, *ACS Appl. Mater. Interfaces* **2017**, *9*, 25073.

[17] R. Borup, J. Meyers, B. Pivovar, Y. S. Kim, R. Mukundan, N. Garland, D. Myers, M. Wilson, F. Garzon, D. Wood, P. Zelenay, K. More, K. Stroh, T. Zawodzinski, J. Boncella, J. E. McGrath, M. Inaba, K. Miyatake, M. Hori, K. Ota, Z. Ogumi, S. Miyata, A. Nishikata, Z. Siroma, Y. Uchimoto, K. Yasuda, K. I. Kimijima, N. Iwashita, *Chem. Rev.* **2007**, *107*, 3904.

[18] R. G. Jungst, G. Nagasubramanian, H. L. Case, B. Y. Liaw, A. Urbina, T. L. Paez, D. H. Doughty, *J. Power Sources* **2003**, *119–121*, 870.

[19] K. Märker, P. J. Reeves, C. Xu, K. J. Griffith, C. P. Grey, *Chem. Mater.* **2019**, *31*, 2545.

[20] H. J. Noh, S. Youn, C. S. Yoon, Y. K. Sun, *J. Power Sources* **2013**, *233*, 121.

[21] S. C. Nagpure, T. R. Tanim, E. J. Dufek, V. V. Viswanathan, A. J. Crawford, S. M. Wood, J. Xiao, C. C. Dickerson, B. Liaw, *J. Power Sources* **2018**, *407*, 53.

**ADVANCED
SCIENCE NEWS**

www.advancedsciencenews.com

**small
methods**

www.small-methods.com

[22] J. Self, C. P. Aiken, R. Petibon, J. R. Dahn, *J. Electrochem. Soc.* **2015**, *162*, A796.

[23] J. Xiao, Q. Li, Y. Bi, M. Cai, B. Dunn, T. Glossmann, J. Liu, T. Osaka, R. Sugiura, B. Wu, J. Yang, J. G. Zhang, M. S. Whittingham, *Nat. Energy* **2020**, *5*, 561.

[24] Y. Zhang, Q. Wang, B. Liaw, S. C. Nagpure, E. J. Dufek, C. C. Dickerson, *J. Electrochem. Soc.* **2020**, *167*, 090502.

[25] S. M. Wood, C. Fang, E. J. Dufek, S. C. Nagpure, S. V. Sazhin, B. Liaw, Y. S. Meng, *Adv. Energy Mater.* **2018**, *8*, 1801427.

[26] X. Ren, L. Zou, X. Cao, M. H. Engelhard, W. Liu, S. D. Burton, H. Lee, C. Niu, B. E. Matthews, Z. Zhu, C. Wang, B. W. Arey, J. Xiao, J. Liu, J. G. Zhang, W. Xu, *Joule* **2019**, *3*, 1662.

[27] S. Kim, A. Raj, B. Li, E. J. Dufek, C. C. Dickerson, H. Y. Huang, B. Liaw, G. M. Pawar, *J. Power Sources* **2020**, *463*, 228180.

[28] A. W. Abboud, E. J. Dufek, B. Liaw, *J. Electrochem. Soc.* **2019**, *166*, A667.

[29] X. Cao, X. Ren, L. Zou, M. H. Engelhard, W. Huang, H. Wang, B. E. Matthews, H. Lee, C. Niu, B. W. Arey, Y. Cui, C. Wang, J. Xiao, J. Liu, W. Xu, J. G. Zhang, *Nat. Energy* **2019**, *4*, 796.